

Fluid registration between lung CT and stationary chest tomosynthesis images

Lin Tian¹, Connor Puett², Peirong Liu¹, Zhengyang Shen¹, Stephen R. Aylward³, Yueh Z. Lee², and Marc Niethammer¹

¹ Department of Computer Science, University of North Carolina at Chapel Hill

² Department of Radiology, University of North Carolina at Chapel Hill

³ Kitware, Inc.

Abstract. Registration is widely used in image-guided therapy and image-guided surgery to estimate spatial correspondences between organs of interest between planning and treatment images. However, while high-quality computed tomography (CT) images are often available at planning time, limited angle acquisitions are frequently used during treatment because of radiation concerns or imaging time constraints. This requires algorithms to register CT images based on limited angle acquisitions. We, therefore, formulate a 3D/2D registration approach which infers a 3D deformation based on measured projections and digitally reconstructed radiographs of the CT. Most 3D/2D registration approaches use simple transformation models or require complex mathematical derivations to formulate the underlying optimization problem. Instead, our approach entirely relies on differentiable operations which can be combined with modern computational toolboxes supporting automatic differentiation. This then allows for rapid prototyping, integration with deep neural networks, and to support a variety of transformation models including fluid flow models. We demonstrate our approach for the registration between CT and stationary chest tomosynthesis (sDCT) images and show how it naturally leads to an iterative image reconstruction approach.

1 Introduction

Image registration is an enabling technology for image-guided interventional procedures (IGP) [7], as it can determine spatial correspondences between pre- and intra-intervention images. Conventionally, pre-interventional images are 3D CT or magnetic resonance (MR) images. Intra-interventional images are typically 2D projective X-rays or ultrasound images [11]. While fast, cheap, and easy to use, these intra-interventional images lack anatomical features and spatial information. It is therefore desirable to combine high-quality 3D pre-intervention images with sDCT [18]. In sDCT, a set of projections is acquired from spatially distributed carbon nanotube-enabled X-ray sources within a limited scanning angle. Given the stationary design, the projections can be acquired fast with high resolution and provide more spatial information than individual X-ray projections. However, this immediately raises the question of how to register a 3D CT to an sDCT volume or its 2D projections.

This may be accomplished by two approaches: (1) reconstructing a 3D image from the 2D projections and proceeding with standard 3D to 3D registration; (2) computing image similarities in the projection space (i.e., by also computing projections from the 3D volume) from which a 3D transformation is inferred. While conceptually simple, the first approach may result in dramatically different 3D image appearances as 3D reconstructions from a small set of projections with a limited scanning angle range will appear blurry and will smear anatomical structures (e.g., the ribs across the lung). Similar appearance differences have been addressed in [21] for rigid transformations via an information-theoretic similarity measure. The second approach is conceptually more attractive in a limited angle setting, as it *simulates* the limited angle acquisitions from the high-quality 3D image. Hence, sets of projection images with *similar* appearance can be compared. Such an approach is called 3D/2D registration. Different 3D/2D registration approaches have been proposed [11], but most only address rigid or affine transformations [1, 4, 8, 9, 21]. Less work considers more flexible transformations or even non-parametric models for 3D/2D registration [3, 16]. A particular challenge is the efficient computation of gradients with respect to the transformation parameters. Zikic et al. [25] establish correspondences between vessels in 3D and a single 2D projection image using a diffusion registration model [13] by exploiting vessel geometry. Prümmer et al. [15, 16] use curvature registration [13] and a similarity measure in projection space based on algebraic image reconstruction. The work by Flach et al. [3] relates most closely to our approach. It is based on Demons registration and digitally reconstructed radiographs (DRR) to compute image similarity in projection space. They propose a sophisticated optimization approach relying on explicit gradient computations. However, gradient computations quickly become unwieldy for complex transformation models which might explain the dearth of 3D/2D models for non-parametric registration. This complexity also hampers flexible modeling and rapid prototyping. Further, while some of the approaches above consider limited numbers of projections, they do not address limited angle acquisitions.

Our starting point for 3D/2D registration is a DRR model for the stationary design of sDCT, which we use to compute image similarity in projection space. In contrast to previous approaches, all our components (the registration model, the similarity measure, and the DRR computation) support automatic-differentiation [5, 14]. This allows focusing our formulation on the forward model and supports the flexible use of our DRR component. Specifically, within one framework we can support a variety of parametric and non-parametric registration models and can also formulate an iterative image reconstruction approach.

Contributions: 1) We propose a differentiable ray-cast DRR generator consistent with sDCT; 2) We propose a 3D/2D registration framework based on these DRR projections which support automatic differentiation. This allows us to easily integrate various registration models (including non-parametric ones) without the need for complex manual gradient calculations; 3) We show how our approach allows for a straightforward implementation of a limited angle image reconstruction algorithm; 4) We demonstrate the performance of our approach

for CT to simulated sDCT registration and explore its performance when varying the number of projections and the range of scanning angles.

2 Ray-cast DRR generator

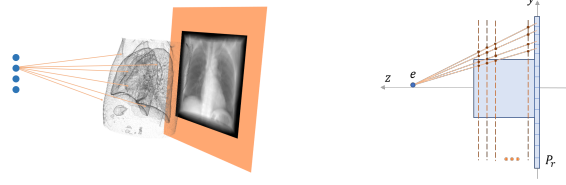


Fig. 1: Illustration of sDCT and our DRR generation. Left: Emitters are spatially distributed in sDCT [18]. Right: Side view of DRR geometry.

Given a high-quality volumetric image $I_0(x)$, $x \in \mathbb{R}^3$ (e.g., based on CT) and one or a set of projection images $I_1(y)$, $y \in \mathbb{R}^2$, we generate DRRs by shooting virtual rays through the 3D volume to a virtual receiver plane P_r of size $W \times H$ (Fig. 1). Assume we are in the coordinate system of the receiver plane whose center is placed and will stay at the origin $(0, 0, 0)$ for all the emitters according to the stationary design of sDCT. The position of points in P_r can then be represented as $p_r = \{(w, h, 0)^T \mid -\frac{W}{2} \leq w \leq \frac{W}{2}, -\frac{H}{2} \leq h \leq \frac{H}{2}\}$. Given an emitter at position $e \in \mathbb{R}^3$ and a point x on the ray from e to p_r , we represent the ray and DRR of this geometry respectively as

$$x = e + \lambda \hat{r}, \quad \hat{r} = \vec{r} / \|\vec{r}\|_2, \quad \vec{r} = p_r - e, \quad I_{proj} = \int I_0(x) dx. \quad (1)$$

We discretize the integral along the z axis of the receiver plane (Fig. 1) and obtain planes $P = z$ parallel to the receiver plane. Given the point $x_z = (0, 0, z)^T$ on the plane with the plane normal $\vec{n} = (0, 0, 1)^T$, any point x on the plane $P = z$ can be written as

$$(x - x_z) \cdot \vec{n} = 0. \quad (2)$$

Combining Eqs. 1 and 2, we obtain the intersection between the ray and the plane $P = z$:

$$x = e + \frac{(x_z - e) \cdot \vec{n}}{\vec{r} \cdot \vec{n}} \vec{r}, \quad (3)$$

The DRR (I_{proj}) can then be written as

$$I_{proj}(w, h, e) = \sum_{z=0}^Z I_0\left(e + \frac{(x_z - e) \cdot \vec{n}}{\vec{r} \cdot \vec{n}} \vec{r}\right) dz, \quad \vec{r} = (w, h, 0)^T - e, \quad dz = \left\| \frac{\vec{r}}{\vec{r} \cdot \vec{n}} \right\|_2. \quad (4)$$

It is possible to write Eq. 4 in tensor form where all rays (for all receiver plane coordinates (w, h)) are evaluated at once. This allows efficient computation on a GPU and only involves tensor products, interpolations, and sums. Hence, we can also efficiently implement derivatives of a DRR with respect to I_0 using automatic differentiation. This allows easy use of DRRs in general loss functions.

3 Registration model

Our goal is to develop a generic 3D/2D registration approach that can be combined with any transformation model. In general, image registration is formulated as an energy minimization problem of the form [13]

$$\theta^* = \arg \min_{\theta} \text{Reg}(\theta) + \lambda \text{Sim}(I_0 \circ \Phi_{\theta}^{-1}, I_1), \quad \lambda > 0, \quad (5)$$

where the transformation Φ_{θ}^{-1} is parameterized by θ , λ is a weighting factor, $\text{Reg}(\theta)$ is a regularizer on the transformation parameters, $\text{Sim}(A, B)$ is a similarity measure (e.g., sum of squared differences, normalized cross correlation, or mutual information) between two images A, B of the same dimension, and I_0, I_1 are the source and target images respectively. Since we are interested in 3D/2D registration, we instead have a 3D source image I_0 and a set of projection target images $\{I_1^i\}$. The similarity measure compares the DRRs of the 3D source image to their corresponding projection images. This changes Eq. 5 to

$$\theta^* = \arg \min_{\theta} \text{Reg}(\theta) + \frac{\lambda}{n} \sum_{i=1}^n \text{Sim}(P^i[I_0 \circ \Phi_{\theta}^{-1}], I_1^i), \quad \lambda > 0, \quad (6)$$

where we now average over the similarity measures with respect to all the n projection images, and $P^i[\cdot]$ denotes the projection consistent with the geometry of the i -th projection image I_1^i (i.e., its DRR). Note that neither the regularizer nor the transformation model changed compared to the registration formulation of Eq. 5. The main difference is that the 3D transformed source image $I_0 \circ \Phi_{\theta}^{-1}$ undergoes different projections and the similarity is measured in the projection space. Clearly, optimizing over such a formulation might be difficult as one needs to determine the potentially rather indirect dependency between the transformation parameter θ , and the image differences measured after projection. While such dependencies have previously been determined analytically [3, 16], they make using advanced registration models and rapid prototyping of registration approaches difficult. Instead, we base our entire registration approach on automatic differentiation. In such a framework, changing the transformation model becomes easy. We explore an affine transformation model ($\Phi_{\theta}^{-1}(x) = Ax + b$, where $\theta = \{A, b\}$, $A \in \mathbb{R}^{3 \times 3}$, $b \in \mathbb{R}^{3 \times 1}$), which has previously been used in 3D/2D registration. To capture large, localized deformations we also use a fluid-registration model after affine pre-registration. We use the large deformation diffeomorphic metric mapping (LDDMM) model [2, 12], where a spatial transformation is parameterized by a spatio-temporal velocity field. The LDDMM

formulation of 3D/2D registration in its shooting form [19, 20, 22] becomes

$$\theta^*(x) = \arg \min_{\theta(x)} \langle \theta, K \star \theta \rangle + \frac{\lambda}{n} \sum_{i=1}^n \text{Sim}(P^i[I_0 \circ \Phi^{-1}(1)], I_1^i), \lambda > 0, \quad (7)$$

$$\Phi_t^{-1} + D\Phi^{-1}v = 0, \quad \Phi^{-1}(0, x) = \Phi_0^{-1}(x), \quad (8)$$

$$m_t + \text{div}(v)m + Dv^T(m) + Dm(v) = 0, \quad v = K \star m, \quad m(x, 0) = \theta(x), \quad (9)$$

where θ is the initial momentum vector field which parameterizes the transformation over time via an advection equation (Eq. 8) on the transformation map Φ^{-1} controlled by the spatially-varying velocity field, v , whose evolution is governed by the Euler-Poincaré equation for diffeomorphisms (EPDiff; Eq. 9); $\Phi^{-1}(1)$ is the transformation at time $t = 1$ which warps the source image and $\Phi_0^{-1}(x)$ is its initial condition (set to the result of our affine pre-registration); K is a regularizer (we choose a multi-Gaussian [17]). This registration model can capture large deformations (as occur in lung registration), is parameterized entirely by its initial momentum field, and can guarantee diffeomorphic transformations. While technically possible, it is easy to appreciate that taking derivatives of the LDDMM 3D/2D registration model is not straightforward. However, our implementation based on automatic differentiation only requires implementation of the forward model (Eqs. 7-9). Gradient computation is then automatic.

Alg. 1 describes our 3D/2D registration algorithm:

Alg. 1: 3D/2D registration

Result: $\theta^*, \Phi_{affine}^{-1}$
Initialize $v = \mathbf{0}$ and $\Phi^{-1}(0) = \Phi_{affine}^{-1}$;
while *loss not converged* **do**
 Compute ϕ^{-1} and warp I_0 using ϕ^{-1} ;
 Compute projection images $\{P^i[I_0 \circ \Phi^{-1}]\}$ using tensor form of Eq. 4;
 Compute $\text{Sim}_{NGF}(P^i[I_0 \circ \Phi^{-1}], I_1^i)$ and $\text{Reg}(\theta)$;
 Back-propagate to compute $\nabla_{\theta} \text{loss}$ and update θ
end

4 Limited angle image reconstruction

We have shown how our DRR model integrates within our 3D/2D registration formulation. Now we apply it for an iterative reconstruction algorithm (Alg. 2).

Given a set of n 2D projection images $\{I^i\}$, our goal is to determine the 3D image I which is most consistent with these projections. Specifically, we solve the following minimization problem:

$$I^* = \arg \min_I \frac{1}{n} \sum_{i=1}^n \text{Sim}(P^i[I], I^i) + \lambda_1 \text{ReLU}(-I) + \frac{\lambda_2}{|\Omega|} \int_{\Omega} \|\nabla I\|_2 \, dx, \quad \lambda_1, \lambda_2 \geq 0, \quad (10)$$

where $P^i[\cdot]$ is the DRR generated for the i -th emitter (Eq. 4). Sim is the L_1 loss between $P^i[I]$ and I^i . We add two regularization terms: 1) $\text{ReLU}(I)$, which

encourages positive reconstructed values, and 2) $\int \|\nabla I\|_2 dx$, which measures the total variation of I , encouraging piece-wise constant reconstructions.

Alg. 2: Iterative reconstruction

Result: I^*
Initialize $I = \mathbf{0}$;
while *loss not converged* **do**
 Compute $\{P^i[I]\}$ using tensor form of Eq. 4;
 Compute $\text{Sim}(P^i[I], I^i)$, $\text{ReLU}(-I)$ and $\int \|\nabla I\|_2 dx$;
 Back-propagate to compute $\nabla_I \text{loss}$ to update I
end

5 Experiments and results

Dataset We use two lung datasets for evaluation: 1) a paired CT-sDCT dataset including raw sDCT projections, 2) a 3D CT dataset with landmarks.

CT-sDCT: We acquired 3 pairs of CT/sDCT images including 31 sDCT projections for each sDCT image with uniformly spaced emitters covering a scanning range of 12 degrees. We use this dataset to test our reconstruction approach.

DIR-Lab 4DCT: This dataset contains 10 pairs of inhale/exhale lung CT images with small deformations and 300 corresponding landmarks per pair. We use this dataset to synthesize corresponding 3D/2D image sets. Specifically, we synthesize projection images from the inspiration phase CT (via our DRR model) and treat them as the target images. As we have the true 3D images with landmarks we can then perform quantitative validation.

5.1 sDCT reconstruction

We compare our reconstruction result (using Alg. 2 and the sDCT projections) to the given sDCT reconstructions (based on [24]) of the CT-sDCT dataset.

Fig. 2 shows the resulting reconstructions. The mean squared error (MSE) between our reconstruction algorithm and the reconstruction algorithm of [24] is small, demonstrating that our method recovers image structure equally well. This result also qualitatively demonstrates the correctness of our DRR projection algorithm.

5.2 3D/2D registrations

Given a CT image and a set of projection images we follow two 3D/2D registration approaches: 1) our approach (Alg. 1) and 2) 3D/3D registration by first reconstructing a 3D volume (Alg. 2) from the set of projection images. The second approach is our baseline demonstrating that the vastly different appearances of the reconstructed 3D volumes (for a low number of projections) and the CT images result in poor registration performance, which can be overcome using our approach. To quantitatively compare both approaches, we use the DIR-Lab

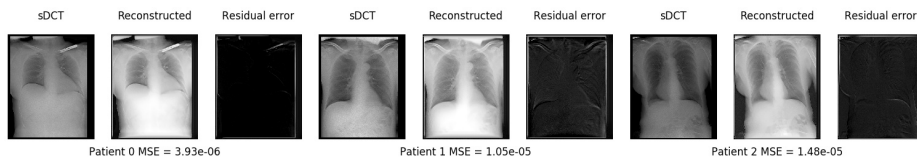


Fig. 2: Comparisons between our reconstructed volumes (Alg. 2) and sDCT volumes (we only show one slice per case). Columns 1, 3, 6: provided sDCT images; columns 2, 5, 8: reconstructed images from our method; columns 3, 6, 9: residual error computed by subtracting our reconstructed image from the sDCT image.

lung CT dataset to create synthetic CT/projection set pairs, where we keep the inspiration phase CT image and create the synthetic DRRs from the expiration phase CT (which constitute our simulated raw sDCT projections). While sDCT imaging is fast, the imaging quality is lower than for CT. For comparison, we provide 3D-CT/3D-CT registration results from the literature.

Tab. 1: Mean distance of expert landmarks before and after registration with our proposed 3D/2D methods and comparison to a SOTA 3D-CT/3D-CT method.

| Dataset | Initial | 3D-2D registration task | | | | 3D-3D reg. task pTVreg [23] |
|---------|---------|-------------------------|-------|------------|-------|-----------------------------------|
| | | Reconstruction | | Projection | | |
| | | Affine | LDDMM | Affine | LDDMM | |
| 4DCT1 | 4.01 | 10.14 | 19.51 | 2.99 | 1.74 | 0.80 |
| 4DCT2 | 4.65 | 19.67 | 29.71 | 2.10 | 1.74 | 0.77 |
| 4DCT3 | 6.73 | 6.07 | 14.90 | 3.11 | 2.24 | 0.92 |
| 4DCT4 | 9.42 | 24.02 | 29.24 | 3.37 | 2.54 | 1.30 |
| 4DCT5 | 7.10 | 19.79 | 26.21 | 4.48 | 2.88 | 1.13 |
| 4DCT6 | 11.10 | 21.81 | 30.51 | 6.13 | 5.18 | 0.78 |
| 4DCT7 | 11.59 | 16.83 | 26.63 | 4.64 | 4.07 | 0.79 |
| 4DCT8 | 15.16 | 14.78 | 18.85 | 7.85 | 2.73 | 1.00 |
| 4DCT9 | 7.82 | 24.44 | 29.04 | 3.70 | 3.76 | 0.91 |
| 4DCT10 | 7.63 | 16.50 | 26.28 | 3.57 | 2.63 | 0.82 |
| Mean | 8.52 | 17.40 | 25.08 | 4.19 | 2.95 | 0.92 |
| Std. | 3.37 | 5.89 | 5.40 | 1.69 | 1.08 | 0.17 |

Registration of 3D-CT/synthetic 2D sDCT projections We resample both expiration/inspiration lung CT images to $1 \times 1 \times 1$ mm. To make our results comparable to state-of-the-art (SOTA) 3D-CT/3D-CT lung registration approaches, we segment the lung and remove all image information outside the lung mask. Then, we create DRRs from the expiration phase lung CT to simulate a set of sDCT projection images with the same emitter geometry as in our CT-sDCT dataset [18]. However, we use only 4 emitters placed evenly within 11 degrees (compared to 31 emitters in CT-sDCT dataset) to assess registration behavior for very few projections. We use $\lambda = 0.5$, the normalized gradient field (NGF) similarity measure [6], stochastic gradient descent optimization for affine registration with $\lambda = 0.01$; and NGF, IBFGS [10] for LDDMM registration. Tab. 1 shows the registration results. As expected, our affine and LDDMM projection results

improve over the initial alignment and LDDMM improves over affine registration, indicating more complex transformations can be recovered with our 3D/2D registration approach. Due to the limited number of projections our results are not as accurate as direct 3D-CT/3D-CT registration (e.g., SOTA pTVreg [?]), which, however, would not be practical in an interventional setting.

Registration of 3D-CT/synthetic sDCT reconstruction We apply Alg. 2 to reconstruct the sDCT from the synthetic projection images of the 3D-CT expiration phase image. We set $\lambda_1 = 100$, $\lambda_2 = 1$ in Eq. 10, then register the 3D-CT to inhale to the reconstructed sDCT using 3D/3D LDDMM registration.

Tab. 1 shows that 3D/2D registration outperforms 3D/3D registration via the reconstructed sDCT. This is because of the vast appearance difference of the sDCT image (compared to 3D-CT), because of limited-angle reconstruction, and because of the low number of projections. In fact, when using the reconstructed sDCT, registration results are worse (for affine and LDDMM) than not registering at all. Hence, using the 3D/2D approach is critical in this setting.

5.3 Influence of angle range and number of projections

We explore how our 3D/2D registration results change with the number of projections (fixing angle range of 11 degrees) and with the angle range (fixing the number of projections at 4). Results are based on DIR-Lab case 4DCT5 (Tab. 1).

Fig. 3 shows that both affine and LDDMM registrations improve as the angle range increases. Note that improvements are most pronounced in the Z direction, which is perpendicular to the receiver plane and thus has the least localization information in such a limited angle imaging setup. Fig. 3 also shows that registration accuracy is relatively insensitive to the number of projections when restricting to a fixed angle range of 11 degrees. This indicates that angle range is more important than the number of projections. Further, when the radiation dose is a concern, larger scanning angles with fewer emitters are preferable.

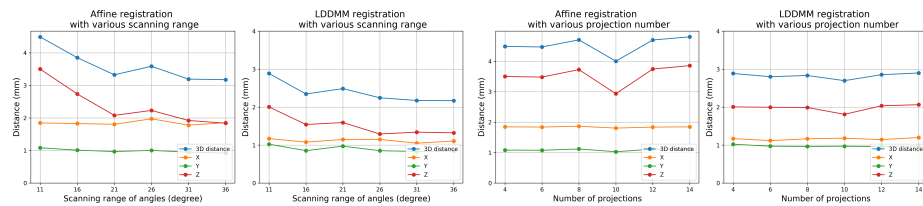


Fig. 3: Influence of angle range and number of projections. First 2 columns: Affine/LDDMM registrations accuracy improves with increasing angle range for 4 projections. Last 2 columns: Affine/LDDMM registration accuracies are relatively insensitive to the number of projections for an 11 degree angle range.

6 Conclusion

We proposed an sDCT-based DRR model and a 3D/2D framework for CT to sDCT registration. Our approach uses automatic differentiation and therefore easily extends to other tasks (e.g., 3D image reconstruction). We demonstrated that DRR-based 3D/2D LDDMM registration outperforms 3D/3D-reconstruction registration in a limited angle setting with small numbers of projections. Future work will extend our approach to an end-to-end 3D/2D deep network registration model. We will also explore alternative image similarity measures and quantitatively validate the approach on real CT/sDCT pairs.

Acknowledgements

Research reported in this work was supported by the National Institutes of Health (NIH) under award number NIH 1-R01-EB028283-01. The content is solely the responsibility of the authors and does not necessarily represent the official views of the NIH.

References

1. Aouadi, S., Sarry, L.: Accurate and precise 2D–3D registration based on x-ray intensity. *Computer vision and image understanding* **110**(1), 134–151 (2008)
2. Beg, M.F., Miller, M.I., Trounev, A., Younes, L.: Computing large deformation metric mappings via geodesic flows of diffeomorphisms. *International journal of computer vision* **61**(2), 139–157 (2005)
3. Flach, B., Brehm, M., Sawall, S., Kachelrieß, M.: Deformable 3D–2D registration for CT and its application to low dose tomographic fluoroscopy. *Physics in Medicine & Biology* **59**(24), 7865 (2014)
4. Fu, D., Kuduvali, G.: A fast, accurate, and automatic 2D–3D image registration for image-guided cranial radiosurgery. *Medical physics* **35**(5), 2180–2194 (2008)
5. Griewank, A., Walther, A.: Evaluating derivatives: principles and techniques of algorithmic differentiation, vol. 105. SIAM (2008)
6. Haber, E., Modersitzki, J.: Intensity gradient based registration and fusion of multi-modal images. In: *International Conference on Medical Image Computing and Computer-Assisted Intervention*. pp. 726–733. Springer (2006)
7. Jaffray, D., Kupelian, P., Djemil, T., Macklis, R.M.: Review of image-guided radiation therapy. *Expert review of anticancer therapy* **7**(1), 89–103 (2007)
8. Jans, H.S., Syme, A., Rathee, S., Fallone, B.: 3D interfractional patient position verification using 2D-3D registration of orthogonal images. *Medical physics* **33**(5), 1420–1439 (2006)
9. Jonic, S., Thévenaz, P., Unser, M.A.: Multiresolution-based registration of a volume to a set of its projections. In: *Medical Imaging 2003: Image Processing*, vol. 5032, pp. 1049–1052. International Society for Optics and Photonics (2003)
10. Liu, D.C., Nocedal, J.: On the limited memory BFGS method for large scale optimization. *Mathematical programming* **45**(1-3), 503–528 (1989)
11. Markelj, P., Tomaževič, D., Likar, B., Pernuš, F.: A review of 3D/2D registration methods for image-guided interventions. *Medical image analysis* **16**(3), 642–661 (2012)

12. Miller, M.I., Trounev, A., Younes, L.: On the metrics and Euler-Lagrange equations of computational anatomy. *Annual review of biomedical engineering* **4**(1), 375–405 (2002)
13. Modersitzki, J.: *Numerical methods for image registration*. Oxford University Press on Demand (2004)
14. Paszke, A., Gross, S., Massa, F., Lerer, A., Bradbury, J., Chanan, G., Killeen, T., Lin, Z., Gimelshein, N., Antiga, L., Desmaison, A., Kopf, A., Yang, E., DeVito, Z., Raison, M., Tejani, A., Chilamkurthy, S., Steiner, B., Fang, L., Bai, J., Chintala, S.: Pytorch: An imperative style, high-performance deep learning library. In: Wallach, H., Larochelle, H., Beygelzimer, A., d'Alché-Buc, F., Fox, E., Garnett, R. (eds.) *Advances in Neural Information Processing Systems* 32, pp. 8024–8035. Curran Associates, Inc. (2019), <http://papers.neurips.cc/paper/9015-pytorch-an-imperative-style-high-performance-deep-learning-library.pdf>
15. Prümmer, M., Han, J., Hornegger, J.: 2D-3D non-rigid registration using iterative reconstruction. In: *Workshop Vision Modeling and Visualization in Erlangen*, <http://www.vmv2005.uni-erlangen.de>. vol. 1, pp. 187–194 (2005)
16. Prümmer, M., Hornegger, J., Pfister, M., Dörfler, A.: Multi-modal 2D-3D non-rigid registration. In: *Medical Imaging 2006: Image Processing*. vol. 6144, p. 61440X. International Society for Optics and Photonics (2006)
17. Risser, L., Vialard, F.X., Wolz, R., Holm, D.D., Rueckert, D.: Simultaneous fine and coarse diffeomorphic registration: application to atrophy measurement in Alzheimer's disease. In: *International Conference on Medical Image Computing and Computer-Assisted Intervention*. pp. 610–617. Springer (2010)
18. Shan, J., Tucker, A.W., Lee, Y.Z., Heath, M.D., Wang, X., Foos, D.H., Lu, J., Zhou, O.: Stationary chest tomosynthesis using a carbon nanotube x-ray source array: a feasibility study. *Physics in Medicine & Biology* **60**(1), 81 (2014)
19. Shen, Z., Vialard, F.X., Niethammer, M.: Region-specific diffeomorphic metric mapping. In: *Advances in Neural Information Processing Systems*. pp. 1096–1106 (2019)
20. Singh, N., Hinkle, J., Joshi, S., Fletcher, P.T.: A vector momenta formulation of diffeomorphisms for improved geodesic regression and atlas construction. In: *2013 IEEE 10th International Symposium on Biomedical Imaging*. pp. 1219–1222. IEEE (2013)
21. Tomazevic, D., Likar, B., Pernus, F.: 3-D/2-D registration by integrating 2-D information in 3-D. *IEEE transactions on medical imaging* **25**(1), 17–27 (2005)
22. Vialard, F.X., Risser, L., Rueckert, D., Cotter, C.J.: Diffeomorphic 3d image registration via geodesic shooting using an efficient adjoint calculation. *International Journal of Computer Vision* **97**(2), 229–241 (2012)
23. Vishnevskiy, V., Gass, T., Szekely, G., Tanner, C., Goksel, O.: Isotropic total variation regularization of displacements in parametric image registration. *IEEE transactions on medical imaging* **36**(2), 385–395 (2017)
24. Wu, G., Inscoe, C., Calliste, J., Lee, Y.Z., Zhou, O., Lu, J.: Adapted fan-beam volume reconstruction for stationary digital breast tomosynthesis. In: *Medical Imaging 2015: Physics of Medical Imaging*. vol. 9412, p. 94123J. International Society for Optics and Photonics (2015)
25. Zikic, D., Groher, M., Khamene, A., Navab, N.: Deformable registration of 3D vessel structures to a single projection image. In: *Medical Imaging 2008: Image Processing*. vol. 6914, p. 691412. International Society for Optics and Photonics (2008)